

UCLA

UCLA Previously Published Works

Title

Structure of Tetrahymena telomerase reveals previously unknown subunits, functions, and interactions

Permalink

<https://escholarship.org/uc/item/6bb6m6k6>

Journal

Science, 350(6260)

ISSN

0036-8075

Authors

Jiang, Jiansen

Chan, Henry

Cash, Darian D

et al.

Publication Date

2015-10-30

DOI

10.1126/science.aab4070

Peer reviewed



Published in final edited form as:

Science. 2015 October 30; 350(6260): aab4070. doi:10.1126/science.aab4070.

## Structure of *Tetrahymena* telomerase reveals previously unknown subunits, functions, and interactions

Jiansen Jiang<sup>1,2,3,\*</sup>, Henry Chan<sup>1,\*</sup>, Darian D. Cash<sup>1</sup>, Edward J. Miracco<sup>1,†</sup>, Rachel R. Ogorzalek Loo<sup>4</sup>, Heather E. Upton<sup>5</sup>, Duilio Cascio<sup>1,6</sup>, Reid O'Brien Johnson<sup>1</sup>, Kathleen Collins<sup>5</sup>, Joseph A. Loo<sup>1,4,6</sup>, Z. Hong Zhou<sup>2,3</sup>, and Juli Feigon<sup>1,3,6,‡</sup>

<sup>1</sup>Department of Chemistry and Biochemistry, University of California, Los Angeles (UCLA), Los Angeles, CA 90095, USA

<sup>2</sup>Department of Microbiology, Immunology, and Molecular Genetics, UCLA, Los Angeles, CA 90095, USA

<sup>3</sup>California Nanosystems Institute, UCLA, Los Angeles, CA 90095, USA

<sup>4</sup>Department of Biological Chemistry, UCLA, Los Angeles, CA 90095, USA

<sup>5</sup>Department of Molecular and Cell Biology, University of California, Berkeley, Berkeley, CA 94720, USA

<sup>6</sup>UCLA–U.S. Department of Energy (DOE) Institute of Genomics and Proteomics, UCLA, Los Angeles, CA 90095, USA

### Abstract

Telomerase helps maintain telomeres by processive synthesis of telomere repeat DNA at their 3'-ends, using an integral telomerase RNA (TER) and telomerase reverse transcriptase (TERT). We report the cryo-electron microscopy structure of *Tetrahymena* telomerase at ~9 angstrom resolution. In addition to seven known holoenzyme proteins, we identify two additional proteins that form a complex (TEB) with single-stranded telomere DNA-binding protein Teb1, paralogous to heterotrimeric replication protein A (RPA). The p75-p45-p19 subcomplex is identified as another RPA-related complex, CST (CTC1-STN1-TEN1). This study reveals the paths of TER in the TERT-TER-p65 catalytic core and single-stranded DNA exit; extensive subunit interactions of the TERT essential N-terminal domain, p50, and TEB; and other subunit identities and structures, including p19 and p45C crystal structures. Our findings provide structural and mechanistic insights into telomerase holoenzyme function.

<sup>‡</sup>Corresponding author. feigon@mbi.ucla.edu.

\*These authors contributed equally to this work.

<sup>†</sup>Present address: Moderna Therapeutics, Cambridge, MA 02141, USA.

#### SUPPLEMENTARY MATERIALS

[www.sciencemag.org/content/350/6260/aab4070/suppl/DC1](http://www.sciencemag.org/content/350/6260/aab4070/suppl/DC1)

Figs. S1 to S10

Tables S1 to S4

References (85–88)

Telomerase is a ribonucleoprotein (RNP) complex that extends the telomere DNA at the 3' ends of linear chromosomes, thereby counteracting the loss of DNA from replication and nucleolytic processing (1, 2). Although telomerase is largely inactive in somatic cells, it is active in stem cells and highly active in most cancer cell lines, where its activity is necessary for their immortal phenotype (3–5). Thus, telomerase is an important regulator of aging, tumorigenesis, and stem cell renewal. Telomerase uses a template contained within the integral telomerase RNA (TER) and a telomerase reverse transcriptase (TERT) to synthesize multiple copies of the G-strand telomere repeat (TTGGGG in ciliates and TTAGGG in vertebrates). Telomerase recruitment to telomeres is regulated by the cell cycle, where its activity requires interplay between telomere end-protection and telomerase proteins (6). Telomere end-maintenance also requires coordinated recruitment of telomerase and DNA polymerase  $\alpha$  for synthesis of the G and C strands, respectively (7, 8). In humans, telomerase is recruited to telomeres by components of shelterin (6). Specifically, the TERT essential N-terminal (TEN) domain interacts with TPP1 (9–11), which, in complex with protection of telomeres 1 (POT1), is a processivity factor (6, 12, 13). The budding yeast telomerase holoenzyme subunit Est3 is a structural homolog of the oligosaccharide/oligonucleotide-binding (OB) fold of TPP1 (14) and, like TPP1, interacts with the TEN domain (15). In addition to recruiting telomerase, the human TPP1-POT1 complex recruits the replication protein A (RPA)-like CST (CTC1-STN1-TEN1) complex. RPA binds sequence-nonspecifically to single-stranded DNA (ssDNA) and plays a central role in DNA replication and repair through protein recruitment (16); CST complexes have been proposed as telomere-specific RPAs (17). CST stimulates DNA polymerase  $\alpha$  for C-strand synthesis and has other diverse functions in different organisms (8, 18–20). Mammalian CST acts as an inhibitor of telomerase action, determines telomeric 3' overhang structure, and plays broader roles in telomere duplex replication and genomewide replication restart (8, 18, 20, 21). Budding yeast CST (Cdc13-Stn1-Ten1) subunit Cdc13 recruits the telomerase holoenzyme to telomeres via interaction of Cdc13 with telomerase subunit Est1, associated with Est3 (22–24).

Telomerase can synthesize telomere repeats in vitro with only TERT and TER, but physiological function requires a variety of other proteins (25, 26). Unlike yeast and mammalian telomerase, *Tetrahymena* telomerase is constitutively assembled (27, 28), making it possible to purify and study all holoenzyme components in a stable complex (29). In addition to TERT and TER, the *Tetrahymena* telomerase holoenzyme contains six other known proteins: p65, p75, p45, p19, p50, and Teb1 (28). TER contains a template/pseudoknot (t/PK) domain, which encloses a template with sequence complementarity to ~1.5 telomere repeats, and a separate activating domain (30). Although TER is essential for activity, the physical arrangement of TER on TERT has remained largely unknown. TERT comprises a telomerase RNA binding domain (TRBD), reverse transcriptase (RT), and C-terminal extension (CTE) that form a TERT “ring” (31), and a separate TEN domain (32) that is important for DNA handling and telomere repeat addition processivity (RAP) (6, 26). p65 binds the TER activating domain [stem-loop 4 (SL4)], inducing a large bend in the RNA that facilitates assembly of TERT with TER to form the RNP catalytic core (33, 34). Teb1 is a paralog of human RPA70, the large subunit of RPA (16, 28). Direct single-stranded telomere DNA binding by Teb1 is necessary for telomerase recruitment to

telomeres (27), where it may compete for binding with the *Tetrahymena* telomere end-binding Pot1a (35). p75, p45, and p19 form a ternary complex whose structure and function remain largely unknown (28). The 25 Å resolution negative-stain electron microscopy (EM) structure and individual subunit affinity labeling revealed the overall architecture of *Tetrahymena* telomerase, where TERT occupies the center of the holoenzyme with p65 bound to SL4 below (29). p50, which forms a central hub linking the TERT-TER-p65 catalytic core, p75-p45-p19, and Teb1, can greatly increase RAP and, with Teb1, can dramatically enhance the rate and processivity of long-product synthesis (29, 36). A detailed mechanistic description of telomerase and its interaction at telomeres has been hampered by a lack of structural models, due to difficulties in obtaining samples of sufficient quantity and quality, as well as subunit complexity and flexibility and low sequence identity among subunits from different organisms. Here we report 9.4 and 8.9 Å cryo-electron microscopy (cryo-EM) structures of *Tetrahymena* telomerase holoenzyme. Combining the cryo-EM structures with data from x-ray crystallography, nuclear magnetic resonance (NMR) spectroscopy, negative-stain EM, and mass spectrometry, we discovered two RPA-related complexes: an RPA paralog TEB, comprising Teb1 and previously undetected proteins Teb2 and Teb3, and a CST complex comprising the previously structurally uncharacterized p75-p45-p19. Both are tethered to p50, a potential structural and functional homolog of TPP1, which in turn binds TERT. A pseudoatomic model of the TERT-TER-p65 catalytic core reveals the path of TER on TERT and the location of the TEN domain, and an exit path for the telomeric repeat DNA is proposed, together providing insights into the enzyme mechanism.

## Cryo-EM reconstruction and overall structure

Telomerase holoenzyme endogenously assembled in *Tetrahymena thermophila* was affinity-purified from a strain bearing a C-terminal 3×Flag (F) and tandem protein A (ZZ) tag on TERT (TERT-FZZ) (29). Cryo-EM specimens of *Tetrahymena* telomerase holoenzyme were prepared using “holey” carbon grids and imaged using a Gatan K2 Summit direct electron detection camera with drift correction (fig. S1). In addition to the preferred front view, particles showed various orientations, which are required for three-dimensional (3D) reconstructions (fig. S2 and methods). Using 40,754 particles, we obtained the intact structure of the *Tetrahymena* telomerase holoenzyme at an overall resolution of 9.4 Å (Fig. 1, A to C, and fig. S1). The negative-stain EM study revealed that the p75-p45-p19 subcomplex is conformationally dynamic (29), which is also apparent in the cryo-EM images (fig. S1, C and D). Therefore, to improve the resolution of the less flexible region, we used a soft mask to exclude the p75-p45-p19 subcomplex from the cryo-EM structure refinement. The resulting reconstruction has an overall resolution of 8.9 Å, with distinguishable secondary structure elements of proteins and RNA (Fig. 1, D to F, and figs. S1 and S3).

Using the features of the secondary structure elements, we were able to rigid-body fit the available atomic-resolution and homology models of protein domains and RNA helical elements (table S1) unambiguously into the 8.9 Å cryo-EM map, except for p75-p45-p19 homologs that were fit into the 9.4 Å cryo-EM map (Fig. 1 and fig. S3). All helical elements of TER—i.e., stem 1 (S1), stem-loop 2 (SL2), SL4, and the pseudoknot (PK)—are clearly

visible with distinct grooves (Fig. 1F), and the path of the single-stranded regions can be approximately traced, although bases cannot be discerned. This allowed us to build a pseudoatomic model of the TERT-TER-p65 catalytic core and Teb1C. The locations of these subunit domains are the same as modeled in the negative-stain EM map within experimental resolution (29), with two exceptions: Teb1C [whose C terminus was correctly localized by Fab labeling (29)] is behind the TEN domain where the PK had been placed, whereas the PK is on the opposite side of TERT by the CTE. In addition, as discussed below, Teb1 forms a heterotrimer with two newly identified proteins, whose location was previously assigned to Teb1C. The p75-p45-p19 ternary complex, whose subunit boundaries could not be determined in the negative-stain EM map (29), is revealed to contain an RPA-like heterotrimer of OB-fold proteins with the domain structure of a CST complex. Overall the pseudoatomic models of the TERT-TER-p65 catalytic core, Teb1-Teb2-Teb3, and p75-p45-p19, which are all linked to p50 in the cryo-EM maps, reveal an intricate network of interactions between the subunits.

### The TER t/PK domain encircles the TERT ring

*Tetrahymena* TERT TRBD-RT-CTE forms a ring-shaped structure and was modeled using the crystal structure of a partial *Tetrahymena* TRBD (residues 259 to 265 and 277 to 519) (37) and a homology model based on the RT-CTE in the *Tribolium* (flour beetle) TERT crystal structure (Fig. 2A) (31, 38). *Tribolium* TERT lacks the TEN domain, and therefore the position of TEN relative to the TERT ring has remained uncertain. Fitting of the *Tetrahymena* TEN domain crystal structure (32) into the cryo-EM map (Fig. 1F) revealed its location on the active-site side of the TERT ring, stacked over the CTE (Fig. 2A and fig. S4A). Residues 640 to 740 of the insertion in fingers domain (IFD) in the RT [which are not modeled, as the *Tribolium* TERT IFD is much shorter than in *Tetrahymena* and other organisms (39, 40)] appear to be near the TEN domain (Figs. 1B and 2A). The evolutionarily nonconserved sequence (residues 178 to 258) that connects TEN to the TERT ring has no available atomic structure and appears undefined in the cryo-EM maps. Consistent with this lack of a fixed conformation, the TEN domain can be assembled in trans with TER and the TERT ring to form an active catalytic core without linker residues 196 to 215 (41, 42).

*Tetrahymena* TER comprises a circular t/PK domain, closed by a short S1, that contains the template, the 3'-flanking template recognition element (TRE), the template boundary element (TBE; also called the TERT binding element), SL2, and PK; and an activating domain (SL4), which is connected to S1 by a short single-stranded linker (Fig. 2B) (30). TER was modeled by fitting previously determined (SL2, p65xRRM:S4, L4) and newly determined (PK) (table S4) NMR structures into the cryo-EM density (see methods). The core t/PK domain encircles the TERT ring approximately perpendicularly, such that the template extends across the bottom of the RT domain on one side of the TERT ring, whereas the PK is on the other side next to the CTE (Fig. 2, C to E, and fig. S4). The bottom of S2 is adjacent to the TRBD CP motif, and the 3' end of the TBE is also near the T motif (Fig. 2C and fig. S4), as predicted (29, 37).

The PK, a conserved element of TER that has been proposed to contribute directly to catalysis (43), is on the opposite side of the TERT ring and far from the active site (~20 Å away) (Fig. 2, C and E, and fig. S4A). The PKs of human and yeast TERs contain conserved interactions that stabilize the PK fold through formation of base triples between loops and stems that are important for activity (43–45). The smaller *Tetrahymena* telomerase PK has two base triples in the NMR structure at 10°C and is not stably folded at higher temperatures in the absence of TERT (46). Based on the position of the PK on TERT, we conclude that, rather than contributing directly to catalysis, the correct PK fold is important for proper positioning of TER on TERT. It is plausible that the PK acts like a watchband ratchet clasp during catalytic core assembly, partially or completely unfolding to allow the TER t/PK domain to fit around the TERT ring and then locking onto the TERT ring by folding of the PK. An indirect effect on assembly may explain why mutations that either stabilize or destabilize the PK, at least for human TER, affect telomerase activity in vitro (45).

Outside of the TER t/PK domain, only L4 in S1/SL4 comes into contact with TERT (Fig. 2, C, E, and F; and fig. S4A). The p65 La-RRM1 binds the 3' polyU tail (33, 47). La-RRM1 has low resolution in the cryo-EM map, probably due to flexibility or partial disassociation (fig. S1), but appears to be associated with both the 3' tail and the 5' end of S1, thereby possibly linking the 3' and 5' ends of TER (Fig. 2E). p65 C-terminal xRRM2 (33) binds to and bends S4, inserting L4 between the end of TRBD helix  $\alpha 8$  and a short helix from the CTE ( $\alpha 22a$ ) that does not exist in *Tribolium* TERT but has well-defined density in the 8.9 Å cryo-EM map (Fig. 2F). In complex with p65, SL4 stimulates activity, hierarchical assembly, and holoenzyme stability (33, 34, 47, 48). L4 binds with high affinity to the TRBD, but its specificity for the CTE remains unknown. A hypothesis consistent with the above, as well as the location of L4 far from the active site and PK, proposes that L4 stabilizes a closed conformation of the TERT ring via specific interactions with TRBD and CTE.

The TER single-stranded region containing TRE, the template, and 3'TBE spans the active-site side of the TERT ring between the CTE and the TEN domain, across the RT, and over the TRBD T/CP pocket, respectively (Fig. 2C). The cryo-EM structure is of telomerase in the apo state before binding telomeric ssDNA. The TRE nucleotides, on the 3' side of the template, pass between the CTE and the TEN domain and could contact the TEN domain. There is clear cryo-EM density for the 3' half of the template only (fig. S3E), suggesting flexible positioning of the 5' residues close to the TBE. Based on the distance from TER S2, the template appears to be positioned near where it would be at the end of telomere repeat synthesis—i.e., the 5' end of the template is closest to the active site. The template also appears to be displaced by ~7 Å from its position at the active site in the crystal structure of *Tribolium* TERT in complex with an RNA-DNA hybrid helix (38), as proposed for the strand-separation step (49). The position of S2/TBE on TERT relative to the 5' end of the template suggests a structural mechanism for template boundary definition. The single-stranded residues of the TBE, which flank S2, wrap on either side of the TERT ring (Fig. 2C and fig. S4B). At the end of telomere repeat synthesis, the S2 and TBE-TRBD interactions could act as an anchor to prevent residues beyond the template from being pulled into the active site (Fig. 2C and fig. S4B).

## Teb1 forms an RPA-like complex with two newly identified proteins

Although Teb1 has four OB-fold domains (N, A, B, and C) (50), only the Teb1C domain and, in some cases, very weak density for Teb1B were apparently visible in the negative-stain EM class averages of *Tetrahymena* telomerase (29). Fitting of Teb1C into the cryo-EM map revealed density of unknown origin in the “knob” next to Teb1C (Fig. 3 and fig. S5A). An exhaustive analysis of the potential positions and fittings of other holoenzyme proteins revealed no known candidates for the knob density (fig. S5A). Because Teb1 is an RPA70 paralog, we investigated whether this part of the cryo-EM map might contain paralogs of the other two RPA subunits (RPA32 and RPA14). We found that the crystal structure of the RPA heterotrimeric core complex (RPA70C-RPA32N-RPA14) (51) fit particularly well into the cryo-EM map, with RPA70C positioned in the cryo-EM density for Teb1C and the RPA32N and RPA14 OB folds in the knob (Fig. 3). RPA trimerization requires the formation of a three- $\alpha$ -helix bundle from the C-termini of RPA70, RPA14, and RPA32N. The predicted C-terminal  $\alpha$  helix of Teb1C is disordered in the crystal structure (50). However, in the cryo-EM map there is clear density of three  $\alpha$  helices involved in the trimerization, with one of them near the C terminus of Teb1C, which we modeled in from the RPA70 structure (Fig. 3 and fig. S3H). To confirm the presence of putative Teb1 heterotrimer proteins in the holoenzyme, we used liquid chromatography–tandem mass spectrometry (LC-MS/MS) to analyze telomerase purified from the TERT-FZZ strain. All seven of the known *Tetrahymena* telomerase proteins, plus two additional hypothetical proteins (THERM\_001113129 and THERM\_00439320) ([www.ciliate.org](http://www.ciliate.org)), were detected with high confidence (table S2A). PSI-BLAST (Position-Specific Iterated Basic Local Alignment Search Tool) (52) searches of corrected cDNA sequences of these 31- and 14-kD proteins showed homology with predicted RPA32 and RPA14 homologs, respectively. Secondary structure predictions by Jpred4 (53) are consistent with an OB fold for the 14-kD protein and an N-terminal OB fold and C-terminal winged-helix (WH) domain for the 31-kD protein. Multiple sequence alignments of these domains with RPA32 and RPA14 orthologs show high similarity (fig. S6). We previously observed that telomerase purified from a *Tetrahymena* strain containing N-terminally ZZF-tagged p50 (F-p50 telomerase) lacks the knob (fig. S5B) and has low RAP, which was attributed to the loss of Teb1 induced by the ZZF-tag on p50 (29). We analyzed F-p50 telomerase by LC-MS/MS and found that the two newly identified proteins and Teb1 are absent (table S2B), which confirms that these two additional proteins are located at the knob in the cryo-EM map and form a complex with Teb1. We conclude that there are two previously undetected proteins in the *Tetrahymena* telomerase holoenzyme that form a heterotrimer with Teb1, here named TEB, paralogous to the ssDNA binding RPA, except specific for telomeric G-strand DNA. In *Tetrahymena*, only the large subunit of RPA, Rfa1, has been identified (54). Transcript expression levels of the two newly discovered Teb1-binding proteins, here named Teb2 and Teb3, are much higher than other telomerase proteins and more similar to the level of Rfa1, as judged by expressed sequence tag abundance (55). These observations suggest that these two subunits may be shared between *Tetrahymena* RPA and TEB.

## Multiple interactions between TEN, TEB, and p50 regulate telomerase activity

The TEN domain has been identified as a major determinant of telomerase activity (6, 42). In addition to its potential TRE interaction (Fig. 2), the cryo-EM map reveals that TEN is adjacent to p50, Teb1C, Teb2N, and the IFD (Fig. 4, A and B). TEN, Teb1C, and p50 contact each other in a triangular arrangement. The Teb1C-TEN interaction is clearly defined in the pseudoatomic models (Fig. 4C). A Teb1 Phe<sup>590</sup>→Ala<sup>590</sup> (F590A)/F648A double mutant was previously shown to ablate purification of telomerase by Teb1-FZZ expressed in cells (27). These two residues of Teb1 are on the Teb1C-TEN interface (Fig. 4C), accounting for the loss of function. In the cryo-EM map, the density of TEN is also in contact with that of Teb2. TEN residues 77 to 87, which are missing in the crystal structure due to disorder (32), might form a structured interface with Teb2N in the holoenzyme (Fig. 4D). In vitro telomerase reconstitution activity assays, which lacked Teb2 and Teb3, showed that deletion of the Teb1C putative C-terminal  $\alpha$  helix (CT $\alpha$ H) had little effect on activity (27, 54). However, purification of Teb1(CT $\alpha$ H)-FZZ expressed in vivo did not recover any telomerase activity or holoenzyme subunits, indicating no in vivo telomerase assembly with Teb1(CT $\alpha$ H) (27). Thus, Teb2 and Teb3, which interact with the Teb1 C-terminal  $\alpha$  helix, likely stabilize association of Teb1 with telomerase.

To provide biochemical evidence for these interactions, we used in vitro reconstitution of complexes with individual TEB subunits expressed in rabbit reticulocyte lysate (RRL) to investigate whether Teb2-TeB3 had any effect on telomerase activity (Fig. 4E). Our activity assays were designed to be sensitive to improved holoenzyme assembly of Teb1 by the use of a very low level of Teb1 expressed in RRL, rather than a saturating concentration of purified bacterially expressed protein, and by purification of RNP from unbound Teb1 before the activity assay. Addition of Teb1 to the catalytic core plus p50 greatly increases RAP, as expected from previous studies (29, 36). Coexpression of Teb2-TeB3 with Teb1 further increased overall activity, consistent with additional stabilization from synergistic interaction of Teb2 with the TEN domain and Teb1C. Addition of Teb2-TeB3 alone, without Teb1, provided no activity enhancement. Together, the cryo-EM structure, activity assays, and in vivo functional studies (27) discussed above support the notion that the TEN-TEB protein interaction network has crucial physiological importance.

The cryo-EM density of p50N appears to contact the TEN domain, as well as Teb1C, the IFD, and p75-p45-p19 (Figs. 1, B and E, and 4A). p50, which has no known sequence or structural homology to other proteins, has a 30-kD N-terminal domain (p50N) that is required for the high level of processive repeat synthesis conferred by p50 binding to the catalytic core (36). Only p50N is apparently visible in the class averages and 3D reconstructions of negative-stain EM images (36) and also in the cryo-EM maps. Like TPP1, p50 contacts the TEN domain (Fig. 4, A and B), and like TPP1-POT1 (13), p50-TeB1 greatly increases RAP (36). These data suggest that p50 could be a structural and functional ortholog to vertebrate TPP1. Although TPP1 was initially identified as a telomere binding protein complex with POT1 bound to the G-strand overhang to block telomerase access, it has emerged as also being the direct mediator of telomerase recruitment, activation, and



homeostasis set-point regulation (6, 7, 56, 57). We fit the structure of the TPP1 OB fold into the 8.9 Å cryo-EM map, but only the characteristic OB-fold b barrel matches well to the cryo-EM density (fig. S3, M to O). This is not surprising, due to the expected cofolding of p50 loops and helices with its interaction partners. Though the fitting does not provide definitive structural homology to TPP1, it does provide evidence that p50N is an OB fold.

The TEN domain has an extensive interface with p50 that apparently includes residues 122 to 127, which are missing in the crystal structure due to disorder (32) (Fig. 4B) and may cofold with p50. We tested whether other TEN domain interactions with p50 inferred from the pseudoatomic model and cryo-EM map were important for RNP activity stimulation by p50, in a manner similar to TEN interactions with TPP1 and Est3. A cluster of residues on human TPP1 (and Est3), called the TEL patch, has been identified as the surface of interaction with TEN (9–11, 14, 56, 57). This interaction is essential for human telomerase recruitment to telomeres. Human TEN residues whose substitution disrupts the interaction of telomerase with TPP1 without greatly affecting catalytic activity have been identified; among these, a direct interaction between Lys<sup>78</sup> (K78) and TPP1 has been demonstrated (57). The equivalent *Tetrahymena* TEN residue based on homology modeling of human TEN with the crystal structure of *Tetrahymena* TEN is K90, which is located near the density for p50 in the cryo-EM map (Fig. 4B). We used our in vitro telomerase reconstitution activity assay to investigate whether K90A at the putative TEN-p50 TEL patch interface imposes a defect in p50 stimulation of telomerase activity (Fig. 4F). K90A had a modest but notable effect on overall activity. The same results were obtained for TEN R137A (R, Arg), which is also located at the TEN-p50 interface in the cryo-EM map. These results support similar interactions between *Tetrahymena* TEN-p50 and human TEN-TPP1. TEN K90A and R137A did not abrogate TEB stimulation of high RAP (Fig. 4F), consistent with direct TEN domain interactions with TEB and p50-bridged TERT-TEB association. TEN residues 112 to 120 form a b hairpin, exclusive to *Tetrahymena* TEN, that inserts at the interface between p50, Teb1C, and Teb2N (Fig. 4B). An adjacent block sequence substitution TEN<sub>(108-113)</sub>NAAIRS (N, Asn; I, Ile; S, Ser) abolishes p50 binding (42). In our experiment, we replaced the b hairpin with GSSG (G, Gly). This substitution abolished p50 activity stimulation, even with added TEB, which is consistent with disruption of both p50 and TEB interactions, but did not affect catalytic core activity. Taken together, these results validate the network of TEN-p50-Teb1C-Teb2N interactions proposed based on the cryo-EM structure (Fig. 4, A to D) and provide supporting evidence that p50 is a structural and functional paralog of TPP1.

The cryo-EM density that we attribute to the IFD appears to independently contact p50 and the TEN domain N terminus, which is disordered in the crystal structure (32) (Figs. 1B and 4A). The IFD is exclusive to TERTs and is important for the translocation step required for RAP (39, 40). We suggest that the human TERT IFD may have parallel, as yet undetected, interactions with the TPP1 OB fold and TEN domains.

### **p75-p45-p19 is a CST complex**

We determined a 2.3 Å x-ray crystal structure of p19 (table S3), which revealed an OB fold most structurally homologous to human Ten1 (Fig. 5A and fig. S7), suggesting the

possibility that p75-p45-p19 might be a CST- or second RPA-like complex. We found that human RPA70C-RPA32N-RPA14, which fit the cryo-EM density of TEB as described above, also fit equally well in the density at the “tip” of the p75-p45-p19 subcomplex in the 9.4 Å cryo-EM map (Fig. 5B). For our model, RPA14 was then replaced with the p19 crystal structure, except for its unstructured C terminus, which forms an  $\alpha$  helix in a three-helix bundle with the other two proteins in the RPA complex (Fig. 5B). p19  $\alpha 2$  and  $\alpha 3$ , which are lacking in RPA14, fit well into the cryo-EM density at the very end of the tip.

The positions of the C-terminal  $\alpha$  helices of RPA70C and RPA14 correspond to the locations of the C termini of p75 and p19 determined by Fab labeling in negative-stain EM (Fig. 5B) (29). We used copurification and limited proteolysis to establish that p45 is composed of an N-terminal domain (p45N) that binds p19 and an independently folded C-terminal domain (p45C) (see methods). These results are consistent with the hypothesis that p45 is a Stn1 or RPA32 homolog. Previous attempts to locate the position of p45 in the holoenzyme by Fab labeling of its C terminus were unsuccessful, as Fab was apparently not visible in negative-stain EM class averages of telomerase holoenzyme (29). Based on the above, we hypothesized that p45C might be connected to p45N in the p75-p45-p19 subcomplex via a flexible linker, and thus Fab-bound p45C was not visible in holoenzyme class averages due to positional flexibility relative to the holoenzyme. We screened >2000 negative-stain EM particles of Fab-labeled p45-F telomerase. The majority had a cluster of three Fab (the 3 $\times$ FLAG tag can bind up to three Fab) located in various positions  $\sim$ 100 Å from the location of p45N (Fig. 5D and fig. S8). The C-terminal domains of RPA32 and Stn1 are composed of WH and tandem WH (WH1-WH2) domains, respectively (17, 19, 58, 59). We determined a 2.4 Å crystal structure of p45C (table S3) and found that it comprises the WH1-WH2 domains (Fig. 5C). The OB fold followed by two WH domains suggests that p45 is a Stn1 homolog (17, 19, 58, 59). Structural alignments (fig. S7), sequence alignments (fig. S6), and phylogenetic cluster analysis (fig. S9) of p19 and p45 domains also support their identification as Ten1 and Stn1 orthologs, despite low sequence homology of CST proteins between kingdoms. In the 9.4 Å cryo-EM map, the remaining unmodeled density in the p75-p45-p19 complex, which appears to contain at least two additional OB folds and contacts p50, can only be attributed to p75 (Fig. 5B). Consistent with this observation, among p75-p45-p19, p75 is necessary and sufficient to bind p50 in vitro (36). There are distinct differences between p75 and Teb1 in terms of their interaction with p50 and their effect on telomerase activity. The cryo-EM maps show that p75 contacts p50 with a domain near its N terminus; in contrast, Teb1 binds p50 and the TEN domain with its C-terminal OB fold. How the potential p75 ortholog CTC1 interacts with telomerase is unknown, but it is interesting to note that the functionally divergent Cdc13 binds yeast telomerase holoenzyme protein Est1 through a recruitment domain adjacent to its N-terminal OB fold (8, 17, 24). In vitro reconstitution assays show that the addition of p75 (or p75-p45-p19) to the catalytic core plus p50 stimulates activity slightly but without an increase in RAP; in contrast, Teb1-p50 interaction stimulates high RAP (29, 36). We conclude that p75-p45-p19 is structurally and functionally distinct from TEB and is most similar to a CST complex. CST has been identified in yeasts, plants, and mammals (8, 19); this is the first evidence for the presence of CST in ciliates.

## The telomeric DNA exits the template toward Teb1C

To obtain information on the path of telomere DNA on telomerase, we prepared a holoenzyme bound to a short telomeric DNA, biotin-5'-d (GTTGGG)<sub>2</sub>GT<sub>L</sub>T<sub>L</sub>G<sub>L</sub>G<sub>L</sub>G, where T<sub>L</sub> and G<sub>L</sub> are locked nucleic acid (LNA) nucleotides (60). For this DNA, six nucleotides (nts) should bind the template and 13 nts should extend out from its 3' end. We then bound biotin with streptavidin, linking two telomerase holoenzymes together via the biotin binding sites in each streptavidin tetramer. Visualization of these dimers of the telomerase holoenzyme by negative-stain EM confirms that the telomere DNA is bound (Fig. 6, A to C). The class averages and 3D reconstructions show clearly visible density of streptavidin located near Teb1C-Teb2N and the putative location of Teb1B (29) on the backside of the telomerase holoenzyme (Fig. 6, B to D). These results reveal that telomeric DNA exits the template from the backside of telomerase and toward Teb1C (Fig. 6D). Furthermore, within the resolution (~30 Å) of negative-stain EM, there is no large-scale structural rearrangement of TERT between the apo structure without DNA and the structure with telomeric DNA bound to the template, consistent with the crystal structure of *Tribolium* TERT without TER (31) versus with an RNA-DNA hairpin mimicking a template-DNA hybrid (38).

## Implications for telomerase catalytic activity and association with telomeres

The cryo-EM structures, p45C and p19 crystal structures, PK NMR structure, domain modeling, and mass spectrometry data presented here reveal a complex RNP composed of three ternary complexes tethered by p50: a TERT-TER-p65 catalytic core; an RPA paralog TEB, comprising Teb1-Teb2-Teb3; and a *Tetrahymena* CST complex comprising p75-p45-p19. TER wraps around the TERT ring and interacts with all four domains of TERT. The TEN domain is close to TER, the TERT ring IFD, p50, Teb1, and Teb2, signaling its importance in the catalytic cycle of telomerase. In addition to the protein domains visible in the cryo-EM map, there are several domains that are not observed due to flexible positioning or intrinsic disorder in the absence of binding partners; these are Teb1 N, A, and B; putative Teb2C, p45C, p50C, p65N; and possibly p75N (schematized in Fig. 7A). Teb1A and Teb1B bind telomere DNA (54), whereas the others (except for p65N) may recruit proteins involved in C-strand synthesis, nucleolytic end-processing, unwinding of G quadruplexes, telomere end-binding, and DNA repair, thereby coordinating telomere maintenance.

In the catalytic core, the TER interactions with TERT are exclusively from the t/PK domain and L4. Because a t/PK and a stem terminus element like L4 are almost universally found in other organisms (2, 30) and TERT is highly conserved, *Tetrahymena* telomerase provides general insights into TER-TERT interactions and assembly. Human TER has a much larger pseudoknot, but the region containing the tertiary stem-loop interactions is comparable in size and probably interacts with TERT at the same location near the CTE, and the human TER t/PK could similarly encircle the TERT ring. This would place the other end of the pseudoknot close to the TEN domain, as implicated biochemically (41). Vertebrate telomerase contains a conserved three-way junction, the CR4-CR5 domain, that binds the

TRBD (61) and has a stem-loop (P6.1) that is critical for activity (62). The P6.1 loop probably inserts at the TRBD-CTE interface (61, 63), similarly to *Tetrahymena* TERL4.

In the cryo-EM structure of apo telomerase presented here, the template is apparently positioned with the 5' end near the active site. This places the 3' end of the template close to Teb1C, where the telomeric DNA binds as it exits the holoenzyme. We suggest that this would facilitate (re)binding of the primer to the template 3' end before translocation. Based on homology with the crystal structures of the RPA-ssDNA complex (51), a model of Teb1AB bound to ssDNA based on the Pot1AB-ssDNA complex (50), and the position of the 5' end of telomeric DNA on telomerase revealed by streptavidin labeling, we can model a possible path of the telomere DNA on telomerase (Fig. 7B). Although the DNA is shown going straight from the template to Teb1, it is possible that during the catalytic cycle the DNA strand may interact with TEN, TRBD, and/or CTE. Within the catalytic core, the TEN domain has been implicated to play a role in ssDNA handling and act as an anchor site (32, 64) and/or in active-site use of the DNA–template RNA hybrid (41). The TEN domain is positioned so that the exiting end of the short DNA–template helix could contact its (unmodeled) N and C termini at the end of a complete telomere repeat synthesis, where this interaction could facilitate template DNA strand separation and help direct the DNA toward Teb1 (fig. S10).

The identification of two RPA related complexes in the *Tetrahymena* telomerase holoenzyme and their constitutive rather than cell-cycle–regulated association allows us to use studies of the *Tetrahymena* telomerase holoenzyme to inform models for interaction and function of human TPP1-POT1 and CST. Like p50-TEN, the interaction between human TPP1 and TEN is essential for bridging telomerase to telomeres (9, 11, 56, 57). Although Teb1C is homologous to RPA70C, Teb1AB is more similar to POT1 (50), which suggests that TEB functions to temporarily prevent rebinding of the telomere-bound Tpt1-Pot1a complex (65). Consistent with the conformational flexibility of p75-p45-p19 around p50 (29), this CST complex could bind the telomeric DNA as it exits Teb1 to recruit DNA polymerase  $\alpha$  for coordinated C-strand synthesis. In summary, the structure of the *Tetrahymena* telomerase catalytic core and identification of telomerase holoenzyme subcomplexes homologous to those found at mammalian, plant, and yeast telomeres provide new mechanistic insights and suggest commonalities of telomerase interaction, action, and regulation at telomeres.

## Materials and methods

### EM specimen preparation and data collection

*Tetrahymena* telomerase holoenzyme was purified following the previously described protocol (29), with some modifications. Briefly, 12 liters of cell culture of TERT-FZZ strain was used for tandem affinity purification following the established procedures (29). The final Flag elution was effected by incubating the telomerase-bound anti-Flag M2 affinity gel with 1.5 ml of elution buffer (20 mM HEPES-NaOH at pH 8.0, 50 mM NaCl, 1 mM MgCl<sub>2</sub>, 1 mM TCEP-HCl, 0.025% IGEPAL CA-630, and 200 ng/μl of 3×Flag peptide) at 4°C. The eluate was incubated with 30 mg of Bio-Beads SM-2 absorbent (Bio-Rad) at 4°C for 2 hours

by end-over-end rotation. The supernatant was then concentrated to 30  $\mu\text{l}$  using a Microcon YM-10 centrifugal filter (Millipore).

For cryo-EM, 2.5  $\mu\text{l}$  of the sample was applied to a glow-discharged Quantifoil R2/1 grid. The grid was blotted with filter paper to remove excess sample and was flash-frozen in liquid ethane with FEI Vitrobot Mark IV. The frozen-hydrated grids were loaded into an FEI Titan Krios electron microscope operated at 300 kV for automated image acquisition with Leginon (66). Micrographs were acquired with a Gatan K2 Summit direct electron detection camera operated in the electron-counting mode at a calibrated magnification of 36,764 $\times$  (pixel size of 1.36  $\text{\AA}$  on the sample level) and defocus values ranging from  $-2.0$  to  $-7.0$   $\mu\text{m}$ . A GIF Quantum LS Imaging Filter (Gatan) was installed between the electron microscope and the K2 camera, but the energy filter (slit) was not used. The dose rate on the camera was set to  $\sim 8$  electrons ( $e^-$ ) per pixel per second, and the total exposure time was 12 s fractionated into 48 frames of images with a 0.25-s exposure time for each frame. Frame images were aligned and averaged for correction of beam-induced drift using the graphics processing unit-accelerated motion correction program (67). The average images from all frames were used for defocus determination and particle picking, and those from the first 28 frames (corresponding to  $\sim 30 e^-/\text{\AA}^2$  of total dose on sample) were used for further data processing, including image classification and 3D structure refinement. A total of 4210 micrographs were used in the data processing.

### Image processing

The defocus value of each cryo-EM micrograph was determined by CTFFIND (68), and the micrographs were corrected for contrast transfer function (CTF) by phase-flipping with the corresponding defocus and astigmatism values using Bsoft (69). A total of 478,698 particles were automatically picked using DoGpicker (70) and windowed out in dimensions of 256 pixels by 256 pixels using batchboxer in EMAN (71). The particles were binned to dimensions of 128 pixels by 128 pixels (pixel size of 2.72  $\text{\AA}$ ) before the following processing. The binned particles were subjected to 2D and 3D classifications by RELION (72), following the recommended procedure ([www2.mrc-lmb.cam.ac.uk/relion/](http://www2.mrc-lmb.cam.ac.uk/relion/)). We performed two consecutive rounds of 2D classifications; in each round, the particles were classified into 100 classes for 25 iterations. After each round of 2D classification, class averages were visually inspected, and particles in the “bad” classes (i.e., those with fuzzy or uninterpretable features or fuzzy density of the p75-p45-p19 subcomplex) (fig. S1B) were removed. About 20% of the class averages were kept after each round of 2D classification, and 47,251 particles were selected for the following 3D classification. The previously obtained negative-stain EM reconstruction at 25  $\text{\AA}$  resolution (29) was low-pass filtered to 60  $\text{\AA}$  to serve as the initial model for 3D classification. The 3D classification generated five classes (fig. S1D), four of which showed an intact holoenzyme structure and were combined into a data set of 40,754 particles for 3D autorefinements by RELION as follows: First, a 3D autorefinement was performed using a spherical mask. The resolution was estimated to be 9.4  $\text{\AA}$  by the relion\_postprocess program using the “gold-standard” Fourier shell correlation at a 0.143 criterion, with a soft mask for which the masking effect was corrected by phase randomization. Second, the density corresponding to the flexible p75-p45-p19 subcomplex was removed from the 9.4  $\text{\AA}$  cryo-EM map using the “Volume Erase” tool in UCSF

Chimera (73), and the resulting map was used to generate a soft-edge mask by the `reliion_mask_create` program. This soft-edge mask was then used in the other 3D autorefinement, in which the p75-p45-p19 subcomplex was excluded during the structure refinement and only included in the final reconstruction. The resolution of this focused refinement was 8.9 Å, estimated as described above. The cryo-EM maps were sharpened with B-factor and low-pass filtered to the stated resolution using the `reliion_postprocess` program. The local resolution was calculated with ResMap (74), using two cryo-EM maps independently refined from halves of data.

*Tetrahymena* telomerase holoenzyme particles adopted a preferred front view in negative-stain EM grids (29) or in cryo-EM Quantifoil grids with holey carbon or coated with continuous carbon film, probably due to its irregular and flattened shape. We tried numerous sample and cryo-EM grid conditions to overcome this preferred orientation problem. The current protocol involving Bio-Beads had the most improved effect on the orientation distribution. However, ~60% of the particles were still in the front view configuration in the cryo-EM images. To assess the effect of preferred orientation on reconstruction resolution, the particles were divided into halves (“uniform” and “preferred”) that showed more uniform or more preferred orientation distribution, respectively (fig. S2). Briefly, the particle orientation file (the “data.star” file generated by RELION 3D autorefinement) of 40,754 particles was analyzed to group particles with the same orientation (same AngleRot and AngleTilt). A threshold of particle count was set so that the particles above the threshold in each orientation group (where the particle count in that group was larger than the threshold) were sent to the preferred half, and the rest were kept in the uniform half. Separation of particles within an orientation group was random. These two halves of the data set were then subjected to 3D autorefinement, using the same parameters as those for the 8.9 Å reconstruction. Comparisons of orientation distributions and 3D reconstructions show that the uniform half had sufficient orientations to obtain a high-quality 3D reconstruction at an overall resolution better than 9.3 Å, and addition of the preferred half only improved the resolution modestly (fig. S2).

### Fitting of atomic models into the cryo-EM maps

For the pseudoatomic model of TERT-TER-p65 and Teb1C, the x-ray crystal and NMR structures of *Tetrahymena* TERT TRBD [Protein Data Bank identification code (PDB ID) 2R4G] (37), TERT TEN (PDB ID 2B2A) (32), Teb1C (PDB ID 3U50) (50), TER SL2 (PDB ID 2FRL) (29), the model of p65 xRRM2:SL4 (33), and the homology model of *Tetrahymena* TERT RT-CTE domains based on *Tribolium* TERT (PDB IDs 3DU6 and 3KYL; TERT CTE residues 1058 to 1117 were not modeled due to low sequence homology to *Tribolium* TERT) (29, 31, 38)—which were previously assembled together by fitting into the negative-stain EM 3D reconstruction (29)—were placed as a whole in an approximate position in the cryo-EM maps, followed by fitting the individual domain structures into the cryo-EM map using the “Fit in Map” function in UCSF Chimera (73). These domain structures or models fit into the cryo-EM map with subtle rotations and translocations, except for Teb1C, which was moved to the cryo-EM density behind TEN and next to TRBD and matched this with high consistency. The PK structure (PDB ID 2N6Q) was manually placed into the cryo-EM density matching its size and shape, as identified by exhaustive

visual inspection of the cryo-EM map, and then fit into the density using UCSF Chimera. S1 was modeled as an ideal A-form helix and fit into cryo-EM density that matched its shape near the PK and SL4. The template was located by fitting the crystal structure of *Tribolium* TERT in complex with an RNA-DNA hybrid helix (PDB ID 3KYL) (38) into the cryo-EM map and finding unmodeled density near the RNA strand. The density assigned for the template is displaced by  $\sim 7$  Å relative to that in the fitted *Tribolium* TERT. The remaining single-stranded regions of TER connecting the above fitted structure elements were modeled into the cryo-EM densities using Coot (75) as follows: First, ideal A-form single-stranded RNA fragments were approximately placed between the flanking high-resolution RNA structures. The bond angles of the RNA backbone were then manually adjusted until the backbone fit into the cryo-EM density that was assigned to the RNA after the protein subunits were fit into the cryo-EM map. Last, standard bond angles and lengths of the backbone of the single-stranded RNA fragments were achieved with the use of the “Regularize Zone” tool in Coot. Because the RNA bases were not distinguishable in the 8.9 Å cryo-EM map, only the backbone of the single-stranded regions was modeled. For the pseudoatomic model of Teb1-Teb2-Teb3, RPA70C:RPA32N:RPA14 from the crystal structure of RPA (PDB ID 1L1O) (51) was fit into the cryo-EM maps by the colores program of Situs, using the exhaustive 6D search algorithm (76). The structure of the RPA trimer fit with high consistency into the cryo-EM map in the density assigned for Teb1C and the adjacent knob. For the final model, RPA70C was replaced by Teb1C, which fits in the same density, except for the C-terminal helix that is disordered in the Teb1C crystal structure but is apparently well ordered in the cryo-EM maps. RPA32N and RPA14 in the model are paralogs of Teb2 and Teb3, respectively. During the Situs fitting of RPA70C:RPA32N:RPA14 to the 9.4 Å cryo-EM map, a second location, corresponding to the tip of the density assigned to the p75-p45-p19 subcomplex, was identified with high confidence, which suggests that it was also an RPA homolog. For the pseudoatomic model of p75C-p45N-p19, RPA14 was manually replaced by p19 (PDB ID 5DFM), except for its C-terminal helix that is disordered in the p19 crystal structure. The crystal structure of the TPP1 OB fold (PDB ID 2I46) (13) was placed in the cryo-EM density assigned to p50N and then fit using UCSF Chimera. The cryo-EM maps and the modeled protein and RNA structures were visualized with UCSF Chimera and PyMOL (77).

### Structure determination of p19, p45C, and TER PK

Full-length p19 (28) was fused via a triple alanine linker to the wild-type maltose binding protein (MBP) vector as described in (78), expressed in *Escherichia coli*, and purified by amylose affinity and size exclusion chromatography (SEC). To obtain diffracting native crystals, a 2:1 mixture of 12 mg/ml of MBP-p19 and the reservoir solution (0.1 M sodium acetate at pH 4.6 and 2.0 M ammonium sulfate) was set up in a 24-well hanging drop format. Full-length p45 (79) was fused to His-tagged MBP via a tobacco etch virus (TEV) protease cleavage site, expressed in *E. coli*, and copurified with cells expressing 6×His-tagged p19 using Ni-nitrilotriacetic acid (NTA) affinity and SEC. p45C (residues 162 to 373) was identified via limited chymotrypsin proteolysis of full-length p45 bound to p19. p45C was fused to His-tagged MBP via the TEV protease cleavage site, expressed in *E. coli*, and purified by Ni-NTA affinity and SEC. To obtain diffracting native crystals, a 1:1 mixture of 14 mg/ml of p45C and the reservoir solution [0.1 M Na-HEPES at pH 7.5, 5%

(v/v) MPD, and 10% (w/v) polyethylene glycol 6000) was set up in a 24-well hanging drop format. Data were collected at 100 K at Advanced Photon Source–Northeastern Collaborative Access Team (APS-NECAT) beamline 24-ID-C on a DECTRIS-PILATUS 6 M pixel detector. Data were indexed, integrated, and scaled using XDS/XSCALE (80). Structures were solved with the molecular replacement program PHASER (81), using initial models from SeMet data sets. Final models were iteratively built and refined in Coot (75) and PHENIX (82). In the crystal structure of p45C,  $\beta 5$  in WH2 is domain-swapped from a neighboring protein in the crystal lattice. This domain-swapped  $\beta 5$  was used to build a biological unit model of p45C (Fig. 5C). NMR assignments were obtained, and solution structure of the TER pseudoknot (nucleotides 68 to 100) was determined following established protocols for human and yeast TER pseudoknots (44, 45, 83). Sample conditions were ~1 mM RNA in 10 mM NaPO<sub>4</sub> at pH 6.3 and 50 mM KCl at 10°C. The structures were calculated with a total of 414 nuclear Overhauser effect distance, 171 dihedral angle, 82 H bond, and 79 residual dipolar coupling restraints using standard protocols in Xplor-NIH 2.9.8. Pairwise root mean square deviation for the 10 lowest-energy structures (out of 100) was 0.83 Å for all heavy atoms (table S4).

### Mass spectrometry

Telomerase was purified from *Tetrahymena* TERT-FZZ and ZZF-p50 strains as described in (29), up to the final anti-FLAG resin wash step before elution. Telomerase was batch-washed on the resin three times by incubation in 1 ml of IGEPAL-free wash buffer at 4°C, rotating end-over-end for 10 min, and was eluted twice by incubation at room temperature with 50 ml of 0.1% trifluoro-acetic acid for 30 min each time. For enzymatic digestion of the samples, 70 ml of deoxycholic acid (0.1% w/v) in 1 M NH<sub>4</sub>HCO<sub>3</sub> was added to the elution. Cysteines were alkylated by adding iodoacetamide to 4 mM and incubating at room temperature. After 30 min, excess dithiothreitol was added to quench residual iodoacetamide, and trypsin (300 ng) was added to initiate digestion. The solution was incubated at 37°C overnight, after which it was acidified to pH 2 with trifluoroacetic acid, to precipitate the deoxycholic acid. The deoxycholic acid was extracted from the aqueous layer with three 200-ml aliquots of water-saturated ethyl acetate (84). The digested peptides were dried and resuspended in 1% formic acid. The resulting tryptic peptides were measured by LC-MS/MS, using an EASY-nLC 1000 (Thermo Scientific, Waltham, MA) coupled to a Q-Exactive Orbitrap mass spectrometer (Thermo Scientific) and an EASY-Spray nano-electrospray ionization source. Peptides were injected onto a 75  $\mu$ m by 15 cm, 3  $\mu$ m, 100 Å PepMap C18 reversed-phase LC column and separated using a linear gradient from 5% solvent B (0.1% formic acid in acetonitrile) and 95% solvent A (0.1% formic acid in water) to 50% solvent B in 2 hours at a constant flow rate of 300 nl/min. Eluted peptides were analyzed with a top-ten data-dependent acquisition method and identified using Proteome Discoverer (version 1.4; Thermo Scientific) coupled to MASCOT (version 2.4.1; Matrix Science, London). Orbitrap MS resolving power was set to 70,000 at a mass/charge ratio ( $m/z$ ) of 200 for MS1 and 17,500 at a  $m/z$  of 200 for MS2. Tryptic peptides with up to two missed cleavages were searched against a *T. thermophila* protein database ([www.ciliate.org](http://www.ciliate.org)) supplemented with common protein contaminant and enzyme sequences (27,046 sequences), with dynamic modifications for carbamidomethyl (C), oxidation (M), deamidation (N, Q), and peptide N-terminal cyclization to eliminate NH<sub>3</sub> (Q, carbamidomethyl-cys) or H<sub>2</sub>O (E)



(C, Cys; M, Met; Q, Gln; E, Glu). Precursor- and product-ion mass tolerances were set to 10 parts per million (or less) and 0.01 daltons, respectively.

### Telomerase reconstitution and activity assays

Telomerase subcomplexes were assembled separately and then combined. The RNP catalytic core was assembled by TERT expression in RRL in the presence of purified bacterially expressed p65 and in vitro transcribed TER. Additional RRL synthesis reactions generated p50N30, Teb1, or coexpressed TEB complex subunits. One subunit was tagged with 3×FLAG (p50N30-F for TEB subunit function studies or TERT-F for TERT TEN domain mutational analysis). Subcomplexes were combined, bound to FLAG antibody resin, and assayed by primer extension as described previously (29), using radiolabeled deoxyguanosine triphosphate (dGTP) and primer (GTTGGG)<sub>3</sub> at a final concentration of 200 nM. Elongation time was 10 min unless otherwise indicated. Products were resolved by denaturing gel electrophoresis, including an end-labeled oligonucleotide added before product precipitation as a recovery control.

### Preparation of DNA-LNA-bound telomerase linked by streptavidin and negative-stain EM

Three-repeat biotinylated LNA/DNA primer was purchased from Exiqon as biotin-5'-GTTGGGG-TTGGGGT<sub>L</sub>T<sub>L</sub>G<sub>L</sub>G<sub>L</sub>G. Telomerase was purified as described (29) from TERT-FZZ strain up to the TEV protease cleavage step, during which 5 mM three-repeat primer and 50 μM dGTP were added to the immunoglobulin G resin. Immediately before the 10-min wash steps of the telomerase-bound flag resin, the resin was split, and one-half was incubated in 50 μl of wash buffer, whereas the other was incubated in 50 μl of wash buffer with 5 μM streptavidin, rotating end-over-end at 4°C for 30 min. Three wash steps were then performed as usual, after which the two resins were recombined and batch-eluted with 3×FLAG peptide, according to the original protocol. Negative-stain EM samples were prepared, imaged, and processed as previously described (29).

### Supplementary Material

Refer to Web version on PubMed Central for supplementary material.

### ACKNOWLEDGMENTS

This work was supported in part by grants from the NIH (GM048123) and NSF (MCB1022379) to J.F., NIH grant GM071940 to Z.H.Z., NIH grant GM103479 to J.A.L., NIH grant R01GM054198 to K.C., American Heart Association postdoctoral fellowship 14POST18870059 to J.J., NIH Ruth L. Kirschstein National Research Service Award (NRSA) postdoctoral fellowship GM101874 to E.J.M., NIH Ruth L. Kirschstein NRSA predoctoral training grant fellowship under GM007185 to H.C. and R.O.J., and NSF Graduate Research Fellowship under DGE-1106400 to H.E.U. We acknowledge support for the NMR core, crystallization core, and x-ray core facilities by DOE grant DE-FC0302ER63421 and the Electron Imaging Center for NanoMachines by NIH grants S10RR23057 and S10OD018111 and NSF DBI-133813. The APS of Argonne National Laboratory is supported by NIH grants P41 RR015301 and P41 GM103403. Use of the APS is supported by DOE under contract DE-AC02-06CH11357. Additional support for EM time was provided to J.F. by National Center for Advancing Translational Sciences UCLA Clinical and Translational Science Institute grant UL1TR000124. We thank M. Sawaya and M. Collazo for help with crystallography and M. Capel, K. Rajashankar, N. Sukumar, F. Murphy, and I. Kourinov of NECAT. The 9.4 and 8.9 Å cryo-EM density maps of *Tetrahymena* telomerase holoenzyme have been deposited in the Electron Microscopy Data Bank under accession numbers EMD-6442 and EMD-6443, respectively. Coordinates and structure factors for the x-ray crystal structures of p19 and p45C have been deposited in the PDB with accession codes 5DFM and 5DFN, respectively. Coordinates and restraints for the solution NMR structure of the TER PK and chemical shifts have been deposited in the PDB (accession code 2N6Q) and Biological

Magnetic Resonance Bank (accession code 25777), respectively. Nucleotide sequence data are available in the third-party annotation (TPA) section of the DNA Data Bank of Japan, European Molecular Biology Laboratory, and GenBank databases under the accession numbers TPA: BK009378 and BK009379.

## REFERENCES AND NOTES

- Blackburn EH, Greider CW, Szostak JW. Telomeres and telomerase: The path from maize, *Tetrahymena* and yeast to human cancer and aging. *Nat. Med.* 2006; 12:1133–1138. doi: 10.1038/nm1006-1133; pmid: 17024208. [PubMed: 17024208]
- Blackburn EH, Collins K. Telomerase: An RNP enzyme synthesizes DNA. *Cold Spring Harbor Perspect. Biol.* 2011; 3:a003558. doi: 10.1101/cshperspect.a003558; pmid: 20660025.
- Armanios M, Blackburn EH. The telomere syndromes. *Nat. Rev. Genet.* 2012; 13:693–704. doi: 10.1038/nrg3246; pmid: 22965356. [PubMed: 22965356]
- Bernardes de Jesus B, Blasco MA. Telomerase at the intersection of cancer and aging. *Trends Genet.* 2013; 29:513–520. doi: 10.1016/j.tig.2013.06.007; pmid: 23876621. [PubMed: 23876621]
- Artandi SE, DePinho RA. Telomeres and telomerase in cancer. *Carcinogenesis.* 2010; 31:9–18. doi: 10.1093/carcin/bgp268; pmid: 19887512. [PubMed: 19887512]
- Nandakumar J, Cech TR. Finding the end: Recruitment of telomerase to telomeres. *Nat. Rev. Mol. Cell Biol.* 2013; 14:69–82. doi: 10.1038/nrm3505; pmid: 23299958. [PubMed: 23299958]
- Stewart JA, Chaiken MF, Wang F, Price CM. Maintaining the end: Roles of telomere proteins in end-protection, telomere replication and length regulation. *Mutat. Res.* 2012; 730:12–19. doi: 10.1016/j.mrfmmm.2011.08.011; pmid: 21945241. [PubMed: 21945241]
- Chen LY, Lingner J. CST for the grand finale of telomere replication. *Nucleus.* 2013; 4:277–282. doi: 10.4161/nucl.25701; pmid: 23851344. [PubMed: 23851344]
- Zhong FL, et al. TPP1 OB-fold domain controls telomere maintenance by recruiting telomerase to chromosome ends. *Cell.* 2012; 150:481–494. doi: 10.1016/j.cell.2012.07.012; pmid: 22863003. [PubMed: 22863003]
- Sexton AN, Youmans DT, Collins K. Specificity requirements for human telomere protein interaction with telomerase holoenzyme. *J. Biol. Chem.* 2012; 287:34455–34464. doi: 10.1074/jbc.M112.394767; pmid: 22893708. [PubMed: 22893708]
- Nandakumar J, et al. The TEL patch of telomere protein TPP1 mediates telomerase recruitment and processivity. *Nature.* 2012; 492:285–289. doi: 10.1038/nature11648; pmid: 23103865. [PubMed: 23103865]
- Xin H, et al. TPP1 is a homologue of ciliate TEBP-b and interacts with POT1 to recruit telomerase. *Nature.* 2007; 445:559–562. doi: 10.1038/nature05469; pmid: 17237767. [PubMed: 17237767]
- Wang F, et al. The POT1-TPP1 telomere complex is a telomerase processivity factor. *Nature.* 2007; 445:506–510. doi: 10.1038/nature05454; pmid: 17237768. [PubMed: 17237768]
- Rao T, et al. Structure of Est3 reveals a bimodal surface with differential roles in telomere replication. *Proc. Natl. Acad. Sci. U.S.A.* 2014; 111:214–218. doi: 10.1073/pnas.1316453111; pmid: 24344315. [PubMed: 24344315]
- Talley JM, DeZwaan DC, Maness LD, Freeman BC, Friedman KL. Stimulation of yeast telomerase activity by the ever shorter telomere 3 (Est3) subunit is dependent on direct interaction with the catalytic protein Est2. *J. Biol. Chem.* 2011; 286:26431–26439. doi: 10.1074/jbc.M111.228635; pmid: 21659533. [PubMed: 21659533]
- Prakash A, Borgstahl GE. The structure and function of replication protein A in DNA replication. *Subcell. Biochem.* 2012; 62:171–196. doi: 10.1007/978-94-007-4572-8\_10; pmid: 22918586. [PubMed: 22918586]
- Lewis KA, Wuttke DS. Telomerase and telomere-associated proteins: Structural insights into mechanism and evolution. *Structure.* 2012; 20:28–39. doi: 10.1016/j.str.2011.10.017; pmid: 22244753. [PubMed: 22244753]
- Chen LY, Redon S, Lingner J. The human CST complex is a terminator of telomerase activity. *Nature.* 2012; 488:540–544. doi: 10.1038/nature11269; pmid: 22763445. [PubMed: 22763445]
- Price CM, et al. Evolution of CST function in telomere maintenance. *Cell Cycle.* 2010; 9:3157–3165. doi: 10.4161/cc.9.16.12547; pmid: 20697207. [PubMed: 20697207]

20. Wu P, Takai H, de Lange T. Telomeric 3' overhangs derive from resection by Exo1 and Apollo and fill-in by POT1b-associated CST. *Cell*. 2012; 150:39–52. doi: 10.1016/j.cell.2012.05.026; pmid: 22748632. [PubMed: 22748632]
21. Wang F, et al. Human CST has independent functions during telomere duplex replication and C-strand fill-in. *Cell Reports*. 2012; 2:1096–1103. doi: 10.1016/j.celrep.2012.10.007; pmid: 23142664. [PubMed: 23142664]
22. Lue NF, Yu EY, Lei M. A popular engagement at the ends. *Nat. Struct. Mol. Biol.* 2013; 20:10–12. doi: 10.1038/nsmb.2483; pmid: 23288360. [PubMed: 23288360]
23. Tucey TM, Lundblad V. Regulated assembly and disassembly of the yeast telomerase quaternary complex. *Genes Dev.* 2014; 28:2077–2089. doi: 10.1101/gad.246256.114; pmid: 25240060. [PubMed: 25240060]
24. Wellinger RJ, Zakian VA. Everything you ever wanted to know about *Saccharomyces cerevisiae* telomeres: Beginning to end. *Genetics*. 2012; 191:1073–1105. doi: 10.1534/genetics.111.137851; pmid: 22879408. [PubMed: 22879408]
25. Egan ED, Collins K. Biogenesis of telomerase ribonucleoproteins. *RNA*. 2012; 18:1747–1759. doi: 10.1261/rna.034629.112; pmid: 22875809. [PubMed: 22875809]
26. Podlevsky JD, Chen JJ. It all comes together at the ends: Telomerase structure, function, and biogenesis. *Mutat. Res.* 2012; 730:3–11. doi: 10.1016/j.mrfmmm.2011.11.002; pmid: 22093366. [PubMed: 22093366]
27. Upton HE, Hong K, Collins K. Direct single-stranded DNA binding by Teb1 mediates the recruitment of *Tetrahymena* thermophila telomerase to telomeres. *Mol. Cell. Biol.* 2014; 34:4200–4212. doi: 10.1128/MCB.01030-14; pmid: 25225329. [PubMed: 25225329]
28. Min B, Collins K. An RPA-related sequence-specific DNA-binding subunit of telomerase holoenzyme is required for elongation processivity and telomere maintenance. *Mol. Cell*. 2009; 36:609–619. doi: 10.1016/j.molcel.2009.09.041; pmid: 19941821. [PubMed: 19941821]
29. Jiang J, et al. The architecture of *Tetrahymena* telomerase holoenzyme. *Nature*. 2013; 496:187–192. doi: 10.1038/nature12062; pmid: 23552895. [PubMed: 23552895]
30. Theimer CA, Feigon J. Structure and function of telomerase RNA. *Curr. Opin. Struct. Biol.* 2006; 16:307–318. doi: 10.1016/j.sbi.2006.05.005; pmid: 16713250. [PubMed: 16713250]
31. Gillis AJ, Schuller AP, Skordalakes E. Structure of the *Tribolium castaneum* telomerase catalytic subunit TERT. *Nature*. 2008; 455:633–637. doi: 10.1038/nature07283; pmid: 18758444. [PubMed: 18758444]
32. Jacobs SA, Podell ER, Cech TR. Crystal structure of the essential N-terminal domain of telomerase reverse transcriptase. *Nat. Struct. Mol. Biol.* 2006; 13:218–225. doi: 10.1038/nsmb1054; pmid: 16462747. [PubMed: 16462747]
33. Singh M, et al. Structural basis for telomerase RNA recognition and RNP assembly by the holoenzyme La family protein p65. *Mol. Cell*. 2012; 47:16–26. doi: 10.1016/j.molcel.2012.05.018; pmid: 22705372. [PubMed: 22705372]
34. Stone MD, et al. Stepwise protein-mediated RNA folding directs assembly of telomerase ribonucleoprotein. *Nature*. 2007; 446:458–461. doi: 10.1038/nature05600; pmid: 17322903. [PubMed: 17322903]
35. Jacob NK, Lescasse R, Linger BR, Price CM. *Tetrahymena* POT1a regulates telomere length and prevents activation of a cell cycle checkpoint. *Mol. Cell. Biol.* 2007; 27:1592–1601. doi: 10.1128/MCB.01975-06; pmid: 17158924. [PubMed: 17158924]
36. Hong K, et al. *Tetrahymena* telomerase holoenzyme assembly, activation, and inhibition by domains of the p50 central hub. *Mol. Cell. Biol.* 2013; 33:3962–3971. doi: 10.1128/MCB.00792-13; pmid: 23918804. [PubMed: 23918804]
37. Rouda S, Skordalakes E. Structure of the RNA-binding domain of telomerase: Implications for RNA recognition and binding. *Structure*. 2007; 15:1403–1412. doi: 10.1016/j.str.2007.09.007; pmid: 17997966. [PubMed: 17997966]
38. Mitchell M, Gillis A, Futahashi M, Fujiwara H, Skordalakes E. Structural basis for telomerase catalytic subunit TERT binding to RNA template and telomeric DNA. *Nat. Struct. Mol. Biol.* 2010; 17:513–518. doi: 10.1038/nsmb.1777; pmid: 20357774. [PubMed: 20357774]

39. Lue NF, Lin YC, Mian IS. A conserved telomerase motif within the catalytic domain of telomerase reverse transcriptase is specifically required for repeat addition processivity. *Mol. Cell. Biol.* 2003; 23:8440–8449. doi: 10.1128/MCB.23.23.8440-8449.2003; pmid: 14612390. [PubMed: 14612390]
40. Xie M, Podlevsky JD, Qi X, Bley CJ, Chen JJ. A novel motif in telomerase reverse transcriptase regulates telomere repeat addition rate and processivity. *Nucleic Acids Res.* 2010; 38:1982–1996. doi: 10.1093/nar/gkp1198; pmid: 20044353. [PubMed: 20044353]
41. Wu RA, Collins K. Human telomerase specialization for repeat synthesis by unique handling of primer-template duplex. *EMBO J.* 2014; 33:921–935. doi: 10.1002/embj.201387205; pmid: 24619002. [PubMed: 24619002]
42. Eckert B, Collins K. Roles of telomerase reverse transcriptase N-terminal domain in assembly and activity of *Tetrahymena* telomerase holoenzyme. *J. Biol. Chem.* 2012; 287:12805–12814. doi: 10.1074/jbc.M112.339853; pmid: 22367200. [PubMed: 22367200]
43. Qiao F, Cech TR. Triple-helix structure in telomerase RNA contributes to catalysis. *Nat. Struct. Mol. Biol.* 2008; 15:634–640. doi: 10.1038/nsmb.1420; pmid: 18500353. [PubMed: 18500353]
44. Cash DD, et al. Pyrimidine motif triple helix in the *Kluyveromyces lactis* telomerase RNA pseudoknot is essential for function in vivo. *Proc. Natl. Acad. Sci. U.S.A.* 2013; 110:10970–10975. doi: 10.1073/pnas.1309590110; pmid: 23776224. [PubMed: 23776224]
45. Theimer CA, Blois CA, Feigon J. Structure of the human telomerase RNA pseudoknot reveals conserved tertiary interactions essential for function. *Mol. Cell.* 2005; 17:671–682. doi: 10.1016/j.molcel.2005.01.017; pmid: 15749017. [PubMed: 15749017]
46. Mihalusova M, Wu JY, Zhuang X. Functional importance of telomerase pseudoknot revealed by single-molecule analysis. *Proc. Natl. Acad. Sci. U.S.A.* 2011; 108:20339–20344. doi: 10.1073/pnas.1017686108; pmid: 21571642. [PubMed: 21571642]
47. O'Connor CM, Collins K. A novel RNA binding domain in *Tetrahymena* telomerase p65 initiates hierarchical assembly of telomerase holoenzyme. *Mol. Cell. Biol.* 2006; 26:2029–2036. doi: 10.1128/MCB.26.6.2029-2036.2006; pmid: 16507983. [PubMed: 16507983]
48. Berman AJ, Gooding AR, Cech TR. *Tetrahymena* telomerase protein p65 induces conformational changes throughout telomerase RNA (TER) and rescues telomerase reverse transcriptase and TER assembly mutants. *Mol. Cell. Biol.* 2010; 30:4965–4976. doi: 10.1128/MCB.00827-10; pmid: 20713447. [PubMed: 20713447]
49. Qi X, et al. RNA/DNA hybrid binding affinity determines telomerase template-translocation efficiency. *EMBO J.* 2012; 31:150–161. doi: 10.1038/emboj.2011.363; pmid: 21989387. [PubMed: 21989387]
50. Zeng Z, et al. Structural basis for *Tetrahymena* telomerase processivity factor Teb1 binding to single-stranded telomeric-repeat DNA. *Proc. Natl. Acad. Sci. U.S.A.* 2011; 108:20357–20361. doi: 10.1073/pnas.1113624108; pmid: 22143754. [PubMed: 22143754]
51. Bochkareva E, Korolev S, Lees-Miller SP, Bochkarev A. Structure of the RPA trimerization core and its role in the multistep DNA-binding mechanism of RPA. *EMBO J.* 2002; 21:1855–1863. doi: 10.1093/emboj/21.7.1855; pmid: 11927569. [PubMed: 11927569]
52. Altschul SF, et al. Gapped BLAST and PSI-BLAST: A new generation of protein database search programs. *Nucleic Acids Res.* 1997; 25:3389–3402. doi: 10.1093/nar/25.17.3389; pmid: 9254694. [PubMed: 9254694]
53. Cole C, Barber JD, J. Barton G. The Jpred 3 secondary structure prediction server. *Nucleic Acids Res.* 2008; 36(suppl. 2):W197–W201. doi: 10.1093/nar/gkn238; pmid: 18463136. [PubMed: 18463136]
54. Min B, Collins K. Multiple mechanisms for elongation processivity within the reconstituted *Tetrahymena* telomerase holoenzyme. *J. Biol. Chem.* 2010; 285:16434–16443. doi: 10.1074/jbc.M110.119172; pmid: 20363756. [PubMed: 20363756]
55. Xiong J, et al. Transcriptome analysis of the model protozoan, *Tetrahymena thermophila*, using deep RNA sequencing. *PLOS ONE.* 2012; 7:e30630. doi: 10.1371/journal.pone.0030630; pmid: 22347391. [PubMed: 22347391]
56. Sexton AN, et al. Genetic and molecular identification of three human TPP1 functions in telomerase action: Recruitment, activation, and homeostasis set point regulation. *Genes Dev.* 2014; 28:1885–1899. pmid: 25128433. [PubMed: 25128433]

57. Schmidt JC, Dalby AB, Cech TR. Identification of human TERT elements necessary for telomerase recruitment to telomeres. *eLife*. 2014; 3:e03563. doi: 10.7554/eLife.03563.
58. Sun J, et al. Stn1-Ten1 is an Rpa2-Rpa3-like complex at telomeres. *Genes Dev*. 2009; 23:2900–2914. doi: 10.1101/gad.1851909; pmid: 20008938. [PubMed: 20008938]
59. Bryan C, Rice C, Harkisheimer M, Schultz DC, Skordalakes E. Structure of the human telomeric Stn1-Ten1 capping complex. *PLOS ONE*. 2013; 8:e66756. doi: 10.1371/journal.pone.0066756; pmid: 23826127. [PubMed: 23826127]
60. Vester B, Wengel J. LNA (locked nucleic acid): High-affinity targeting of complementary RNA and DNA. *Biochemistry*. 2004; 43:13233–13241. doi: 10.1021/bi0485732; pmid: 15491130. [PubMed: 15491130]
61. Huang J, et al. Structural basis for protein-RNA recognition in telomerase. *Nat. Struct. Mol. Biol*. 2014; 21:507–512. doi: 10.1038/nsmb.2819; pmid: 24793650. [PubMed: 24793650]
62. Chen JL, Opperman KK, Greider CW. A critical stem-loop structure in the CR4-CR5 domain of mammalian telomerase RNA. *Nucleic Acids Res*. 2002; 30:592–597. doi: 10.1093/nar/30.2.592; pmid: 11788723. [PubMed: 11788723]
63. Bley CJ, et al. RNA-protein binding interface in the telomerase ribonucleoprotein. *Proc. Natl. Acad. Sci. U.S.A.* 2011; 108:20333–20338. doi: 10.1073/pnas.1100270108; pmid: 22123986. [PubMed: 22123986]
64. Zaug AJ, Podell ER, Cech TR. Mutation in TERT separates processivity from anchor-site function. *Nat. Struct. Mol. Biol*. 2008; 15:870–872. doi: 10.1038/nsmb.1462; pmid: 18641663. [PubMed: 18641663]
65. Linger BR, Morin GB, Price CM. The Pot1a-associated proteins Tpt1 and Pat1 coordinate telomere protection and length regulation in *Tetrahymena*. *Mol. Biol. Cell*. 2011; 22:4161–4170. doi: 10.1091/mbc.E11-06-0551; pmid: 21900503. [PubMed: 21900503]
66. Suloway C, et al. Automated molecular microscopy: The new Legimon system. *J. Struct. Biol*. 2005; 151:41–60. doi: 10.1016/j.jsb.2005.03.010; pmid: 15890530. [PubMed: 15890530]
67. Li X, et al. Electron counting and beam-induced motion correction enable near-atomic-resolution single-particle cryo-EM. *Nat. Methods*. 2013; 10:584–590. doi: 10.1038/nmeth.2472; pmid: 23644547. [PubMed: 23644547]
68. Mindell JA, Grigorieff N. Accurate determination of local defocus and specimen tilt in electron microscopy. *J. Struct. Biol*. 2003; 142:334–347. doi: 10.1016/S1047-8477(03)00069-8; pmid: 12781660. [PubMed: 12781660]
69. Heymann JB, Belnap DM. Bsoft: Image processing and molecular modeling for electron microscopy. *J. Struct. Biol*. 2007; 157:3–18. doi: 10.1016/j.jsb.2006.06.006; pmid: 17011211. [PubMed: 17011211]
70. Voss NR, Yoshioka CK, Radermacher M, Potter CS, Carragher B. DoG Picker and TiltPicker: Software tools to facilitate particle selection in single particle electron microscopy. *J. Struct. Biol*. 2009; 166:205–213. doi: 10.1016/j.jsb.2009.01.004; pmid: 19374019. [PubMed: 19374019]
71. Ludtke SJ, Baldwin PR, Chiu W. EMAN: Semiautomated software for high-resolution single-particle reconstructions. *J. Struct. Biol*. 1999; 128:82–97. doi: 10.1006/jsbi.1999.4174; pmid: 10600563. [PubMed: 10600563]
72. Scheres SH. RELION: Implementation of a Bayesian approach to cryo-EM structure determination. *J. Struct. Biol*. 2012; 180:519–530. doi: 10.1016/j.jsb.2012.09.006; pmid: 23000701. [PubMed: 23000701]
73. Pettersen EF, et al. UCSF Chimera—A visualization system for exploratory research and analysis. *J. Comput. Chem*. 2004; 25:1605–1612. doi: 10.1002/jcc.20084; pmid: 15264254. [PubMed: 15264254]
74. Kucukelbir A, Sigworth FJ, Tagare HD. Quantifying the local resolution of cryo-EM density maps. *Nat. Methods*. 2014; 11:63–65. doi: 10.1038/nmeth.2727; pmid: 24213166. [PubMed: 24213166]
75. Emsley P, Cowtan K. Coot: Model-building tools for molecular graphics. *Acta Crystallogr. D*. 2004; 60:2126–2132. doi: 10.1107/S0907444904019158; pmid: 15572765. [PubMed: 15572765]
76. Chac'n P, Wriggers W. Multi-resolution contour-based fitting of macromolecular structures. *J. Mol. Biol*. 2002; 317:375–384. doi: 10.1006/jmbi.2002.5438; pmid: 11922671. [PubMed: 11922671]

77. The PyMOL Molecular Graphics System, Version 1.7.4. Schrödinger, LLC.
78. Moon AF, Mueller GA, Zhong X, Pedersen LC. A synergistic approach to protein crystallization: Combination of a fixed-arm carrier with surface entropy reduction. *Protein Sci.* 2010; 19:901–913. pmid: 20196072. [PubMed: 20196072]
79. Witkin KL, Collins K. Holoenzyme proteins required for the physiological assembly and activity of telomerase. *Genes Dev.* 2004; 18:1107–1118. doi: 10.1101/gad.1201704; pmid: 15131081. [PubMed: 15131081]
80. Kabsch W. Integration, scaling, space-group assignment and post-refinement. *Acta Crystallogr. D.* 2010; 66:133–144. doi: 10.1107/S0907444909047374; pmid: 20124693. [PubMed: 20124693]
81. McCoy AJ, et al. Phaser crystallographic software. *J. Appl. Cryst.* 2007; 40:658–674. doi: 10.1107/S0021889807021206; pmid: 19461840. [PubMed: 19461840]
82. Afonine PV, et al. Towards automated crystallographic structure refinement with phenix.refine. *Acta Crystallogr. D.* 2012; 68:352–367. doi: 10.1107/S0907444912001308; pmid: 22505256. [PubMed: 22505256]
83. Kim NK, et al. Solution structure and dynamics of the wild-type pseudoknot of human telomerase RNA. *J. Mol. Biol.* 2008; 384:1249–1261. doi: 10.1016/j.jmb.2008.10.005; pmid: 18950640. [PubMed: 18950640]
84. Erde J, Loo RR, Loo JA. Enhanced FASP (eFASP) to increase proteome coverage and sample recovery for quantitative proteomic experiments. *J. Proteome Res.* 2014; 13:1885–1895. doi: 10.1021/pr4010019; pmid: 24552128. [PubMed: 24552128]

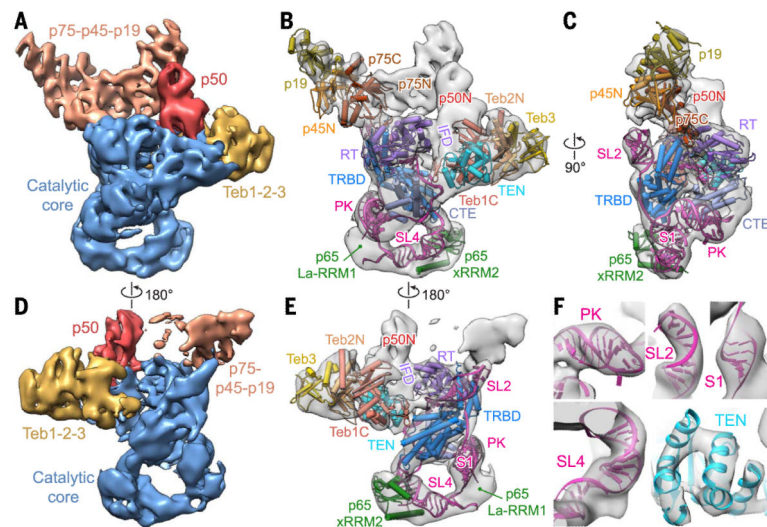


**Fig. 1. Cryo-EM reconstructions of *Tetrahymena* telomerase holoenzyme**  
 (A) Front view of the 9.4 Å cryo-EM map, with the catalytic core, Teb1C-Teb2N-Teb3 (TEB), p75C-p45N-p19 (CST), and p50N colored in blue, gold, copper, and red, respectively. (B) Front view of the 9.4 Å cryo-EM map (gray surface) with pseudoatomic models of the TERT-TER-p65 catalytic core, Teb1C-Teb2N-Teb3, and p75C-p45N-p19. (C) Side view of the cryo-EM map and pseudoatomic models shown in (B). (D) Back view of the 8.9 Å cryo-EM map colored as in (A). (E) Back view of the 8.9 Å cryo-EM map, showing pseudoatomic models of TERT-TER-p65 and Teb1C-Teb2N-Teb3. (F) Close-up views of fitting of TER helical domains PK, SL2, S1, and SL4 and TEN domain into the 8.9 Å cryo-EM map. TERT domains are TEN (cyan), TRBD (dark blue), RT (violet, with IFD labeled in violet), and CTE (light blue). Other proteins and TER are colored individually.

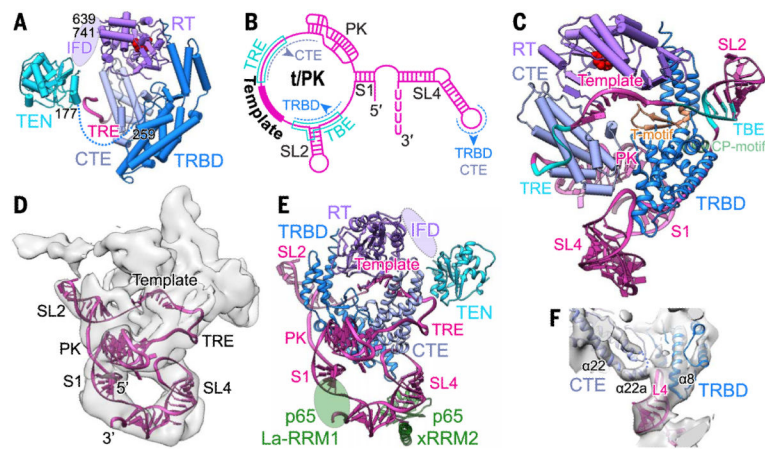


**Fig. 2. Structure of the TERT-TER-p65 catalytic core**

(A) Model structure of TERT, showing the putative IFD (light violet), active-site catalytic triad residues (red), linker (dotted blue line), and TER TRE. (B) Secondary structure of TER. Locations of CTE and TRBD on TER are indicated with dotted lines. (C) Pseudoatomic model of TERT ring-TER, showing TBE-template-TRE and L4 on TERT, viewed from the active-site side of TERT. (D) Front view of the 8.9 Å cryo-EM map, showing a pseudoatomic model of TER. (E) Front view of the pseudoatomic model TERT-TER-p65 catalytic core. The putative location of IFD is shown as violet oval. (F) A region of the 8.9 Å cryo-EM map and pseudoatomic model showing L4 at the interface of TRBD (helix  $\alpha 8$ ) and CTE (helix  $\alpha 22a$ , residues 975 to 983). The numbering of *Tetrahymena* TERT secondary structure elements follows that of the *Tribolium* TERT structure.



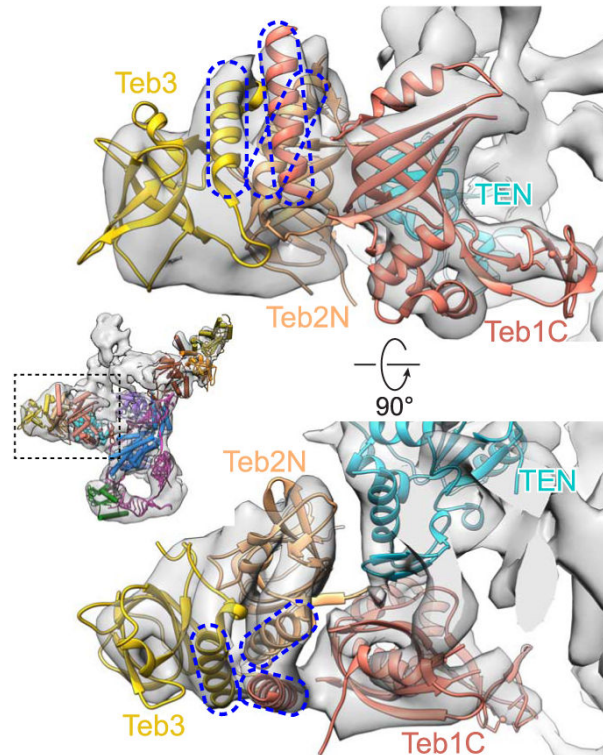


**Fig. 3. Identification of two previously unknown holoenzyme proteins, Teb2 and Teb3**  
 Shown are two views of the knob and Teb1C region of the 8.9 Å cryo-EM map with a model of Teb1C-Teb2N-Teb3 based on fitting of RPA70C-RPA32N-RPA14 into the cryo-EM map, followed by replacement of RPA70C with Teb1C, except for the RPA70C C-terminal  $\alpha$  helix. The TEN domain is shown in cyan. The three-helix bundle between the C-terminal residues of Teb1C, Teb2N, and Teb3 (modeled from RPA) is highlighted with dashed lines. The inset shows the corresponding back view of the holoenzyme for reference.

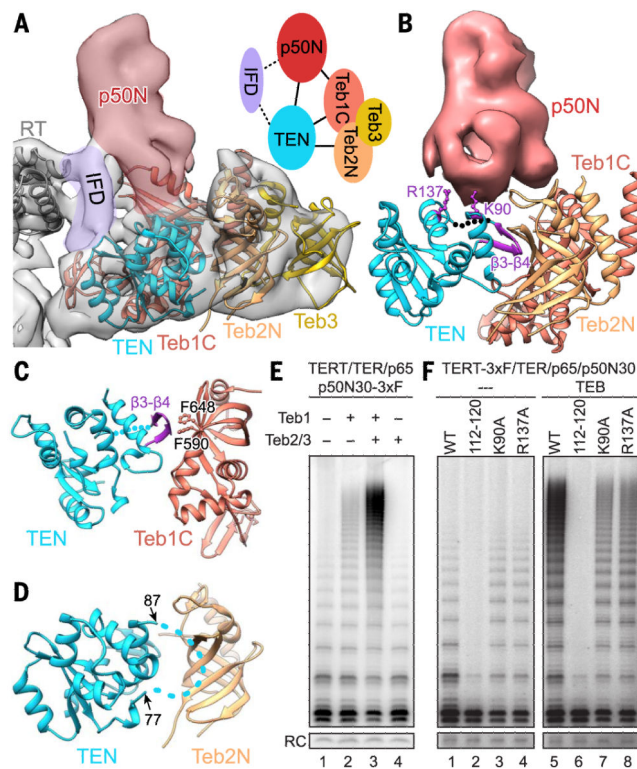


**Fig. 4. Subunit interactions between p50, TEN, IFD, Teb1C, Teb2N, and Teb3**

(A) Region of the 8.9 Å cryo-EM map showing density linking p50N, TEN, IFD, and TEB. The inset shows a schematic of the interactions. Dotted lines represent inferred interactions from the cryo-EM density and atomic models fitted to the cryo-EM map. (B) Interactions between p50N (red, cryo-EM density), TEN, Teb1C, and Teb2N. The TEN residue K90 side chain corresponding to the human TEN domain residue K78 that interacts with TPP1, R137, and the  $\beta$ 3- $\beta$ 4 hairpin (residues 112 to 120) is highlighted in violet. (C) Interactions between TEN and Teb1C. Teb1C F590/F648 residues (orange stick) that together abrogate the Teb1C-TEN interaction and the TEN  $\beta$ 3- $\beta$ 4 hairpin (violet) are indicated. TEN residues 122 to 127, disordered in the crystal structure, are represented by dotted lines in (B) and (C). (D) Interactions between TEN and Teb2N. TEN residues 77 to 87, disordered in the crystal structure, are shown as a dashed line. Pseudoatomic models of TEN, Teb1C, and Teb2N interactions are based on crystal structures of TEN, Teb1C, and RPA32N-RPA14 fit into the 8.9 Å cryo-EM map. (E and F) In vitro reconstitution telomerase activity assays for the effect of (E) TEB proteins and (F) TEN domain mutations on the catalytic core assembled with p50N30. TEN domain mutations were tested without (lanes 1 to 4) and with (lanes 5 to 8) TEB. WT, wild type; RC, recovery control.

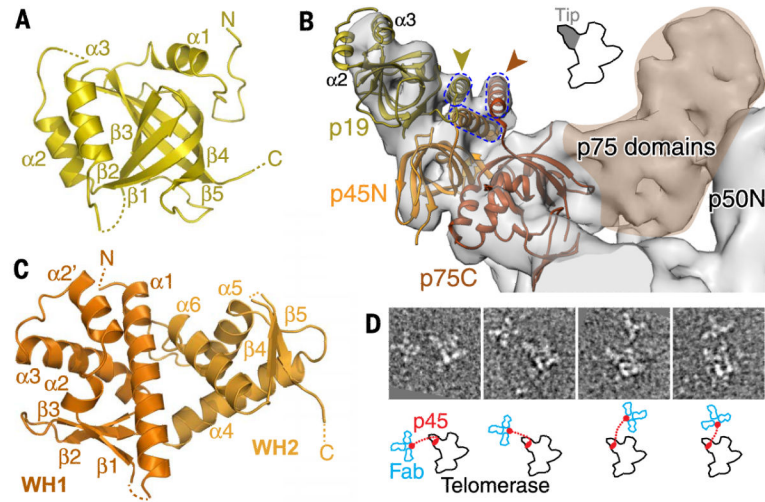


**Fig. 5. Identification of p75-p45-p19 as a *Tetrahymena* CST complex**

(A) Crystal structure of p19, an OB fold. (B) Model of p75C-p45N-p19 based on fitting of RPA70C-RPA32N-RPA14 into the 9.4 Å cryo-EM map, followed by replacement of RPA14 by p19, except for the RPA14 C-terminal helix. p19  $\alpha 2$  and  $\alpha 3$  account for the density at the end of the tip. Gold and orange arrowheads point to the locations of the p19 and p75 C termini, respectively, previously determined by Fab labeling in negative-stain EM (29). The three-helix bundle between the C-terminal residues of p75, p45N, and p19 (modeled from RPA) is illustrated with dashed lines. (C) Crystal structure of p45C, a WH-WH domain.  $\beta 5$  is domain-swapped from a neighboring protein in the crystal lattice. (D) (Top) Negative-stain EM images of four typical p45-Fab-labeled telomerase holoenzyme particles, showing a cluster of 3 Fab bound to the C terminus of p45 at various locations near the holoenzyme. The side length of each image box is 44 nm. (Bottom) Corresponding outlines of telomerase and Fabs are shown in black and blue, respectively. Red dots indicate the p45C (attached to 3 Fab) and p45N (on telomerase) domains; dotted lines represent the linker.

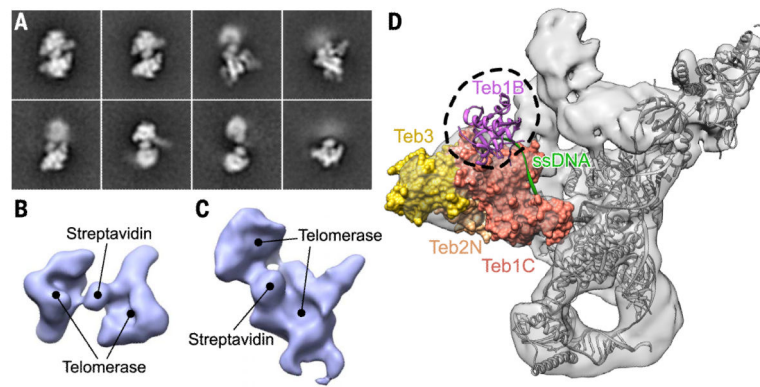


**Fig. 6. Telomere ssDNA exits from the backside of the *Tetrahymena* telomerase holoenzyme** (A) Negative-stain EM class averages of the telomerase holoenzyme dimerized by primer-biotin-streptavidin-biotin-primer. The side length of each image box is 42 nm. (B and C) Random conical tilt (RCT) reconstruction of dimeric telomerase holoenzymes. One of two telomerase holoenzymes in (C) shows uninterpretable features due to flexible positioning of the two holoenzymes relative to each other. (D) A 9.4 Å cryo-EM map of the telomerase holoenzyme (gray surface) and the position of primer-attached streptavidin (black dashed circle), as identified by negative-stain EM RCT reconstruction in (B) and (C). Teb1B (purple) and ssDNA (green) exiting through Teb1C are modeled by fitting the crystal structure of the RPA:ssDNA complex (PDB ID 4GNX).

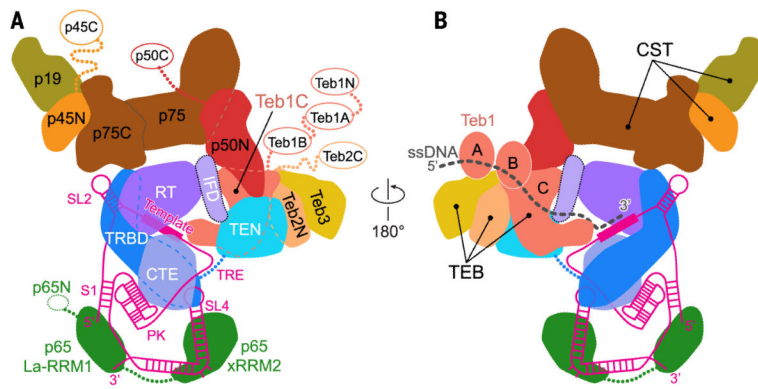


**Fig. 7. Schematics of the complete *Tetrahymena* telomerase holoenzyme and DNA exit path**  
**(A)** Arrangement of the subunits and domains of the *Tetrahymena* telomerase catalytic core, TEB, and CST complexes tethered to p50, shown as front view. Domains connected by flexible linkers and not seen in the cryo-EM map are shown with oval outlines. **(B)** Arrangement of the holoenzyme with proposed path of telomere ssDNA, shown as back view. Teb1AB domains are presumed to be ordered when DNA-bound.